Self-diffusion in dense granular shear flows

Brian Utter* and R. P. Behringer
Department of Physics and Center for Nonlinear and Complex Systems, Box 90305, Duke University, Durham, North Carolina 27708, USA
(Received 22 August 2003; published 31 March 2004)

Diffusivity is a key quantity in describing velocity fluctuations in granular materials. These fluctuations are the basis of many thermodynamic and hydrodynamic models which aim to provide a statistical description of granular systems. We present experimental results on diffusivity in dense, granular shear flows in a two-dimensional Couette geometry. We find that self-diffusivities D are proportional to the local shear rate $\dot{\gamma}$ with diffusivities along the direction of the mean flow approximately twice as large as those in the perpendicular direction. The magnitude of the diffusivity is $D \approx \dot{\gamma} a^2$, where a is the particle radius. However, the gradient in shear rate, coupling to the mean flow, and strong drag at the moving boundary lead to particle displacements that can appear subdiffusive or superdiffusive. In particular, diffusion appears to be superdiffusive along the mean flow direction due to Taylor dispersion effects and subdiffusive along the perpendicular direction due to the gradient in shear rate. The anisotropic force network leads to an additional anisotropy in the diffusivity that is a property of dense systems and has no obvious analog in rapid flows. Specifically, the diffusivity is suppressed along the direction of the strong force network. A simple random walk simulation reproduces the key features of the data, such as the apparent superdiffusive and subdiffusive behavior arising from the mean velocity field, confirming the underlying diffusive motion. The additional anisotropy is not observed in the simulation since the strong force network is not included. Examples of correlated motion, such as transient vortices, and Lévy flights are also observed. Although correlated motion creates velocity fields which are qualitatively different from collisional Brownian motion and can introduce nondiffusive effects, on average the system appears simply diffusive.

DOI: 10.1103/PhysRevE.69.031308 PACS number(s): 45.70.Mg, 45.05.+x, 45.70.−n

I. INTRODUCTION

A. Overview

Despite the prevalence of granular materials in nature and industry, a coherent understanding of granular flows is still lacking. Particularly in dense systems, features such as jamming, shear bands, and the coexistence of solidlike and liquidlike regions make it difficult to offer a simple theoretical description. Fluctuations in both the force network and particle velocities can be of the same magnitude as the mean values and are known to be important aspects of the microscopic behavior of dense granular flows [1]. Due to the complexity of these systems, one of the key goals of current research is to develop a statistical description of steady state behavior, such as a thermodynamic or hydrodynamic model. Fundamental to statistical approaches is understanding the mean fluctuating part of particle motion, which is described by a granular diffusivity.

Sheared granular systems have received considerable attention recently [1–3] as an important example of granular flow. Diffusion, in particular, has been studied in a variety of granular systems, such as vibrated grains [4,5], tumblers [6,7], chute flows [8–10], and sheared systems [11–19], but these studies have predominantly focused on rapid flow regimes. Understanding slow, high density, flow is not trivial [18]; there is no replacement at the fundamental level for collisionally based kinetic theories that are expected to apply only in the dilute rapid flow regime.

In this paper, we characterize the self-diffusivity of grains in a two-dimensional (2D) Couette shearing experiment by studying individual particle trajectories over time. In contrast to most previous results, we focus on quasistatic dense flows. In this regime, since particles are constantly in contact with their neighbors, interactions are not collisional and material flow is largely confined to a shear band with a nominal thickness on the order of 5 particle diameters.

Several observations from the present experiments are noteworthy: (1) We find that particle diffusivity is proportional to the local shear rate, with diffusivities approximately twice as large along the mean flow direction as the perpendicular direction. (2) We show that unlike rapid flows, the anisotropic force network induces a substantial anisotropy in the diffusivity. This is in addition to the usual anisotropy induced by the direction of mean flow. (3) Care must be taken when calculating diffusivities in a shear gradient [20], as motion can appear to be subdiffusive or superdiffusive due to a gradient in the shear rate or Taylor dispersion [21]. We show through a simple Fokker-Planck model that apparent subdiffusive or superdiffusive behavior can be attributed to shear gradient and boundary effects. (4) Hence, the grain motion is statistically consistent with a simple random walk in the presence of shear gradients. (5) Nevertheless, at larger spatial scales, we occasionally observe correlated motion and Lévy flights. But these events are rare and do not have a significant impact in the mean.

B. Models for granular diffusion

In the kinetic theory approach, a granular temperature is often defined as $T \propto \langle (v - \bar{v})^2 \rangle$, with instantaneous particle

*Electronic address: utter@phy.duke.edu

velocity v and mean velocity $\overline{v}$, in which the velocity fluctuations contribute to a temperature in analogy with molecular gases.

A different approach was recently proposed by Makse and Kurchan, who applied uniform shear in a numerical experiment and measured diffusivity D and mobility χ to define a temperature D/χ by analogy with fluid systems [14]. In their model, they report that the 0th law (thermal equilibration) is satisfied in a bidisperse mixture, supporting the thermodynamic picture. This is in contrast to experimental measurements of kinetic granular temperature which find a lack of equipartition when different types of particles are present [22,23].

Isotropic Brownian diffusion in an unbounded system is often characterized by the time evolution of the second moments of a probability distribution function (PDF). For example,

$$\langle x^2 \rangle = 2Dt, \tag{1}$$

where x is the particle position relative to its initial position ($v \equiv \Delta x/\Delta t$ for a small time step Δt), D is the diffusivity, and t is time.

More generally, diffusion must be described by a tensor. For instance, diffusivities along the flow direction in granular gases are in general different from transverse diffusivities [12,17,18].

Diffusion in even a simple shear flow is complicated by Taylor dispersion effects [21], in which diffusive motion couples to the mean flow leading to larger dispersion along the flow direction, as recently elucidated in systems of noncolloidal particles [20]. In this case, $\langle x^2 \rangle$ is nonlinear in time, i.e., it contains higher order corrections due to the coupling of the shear to the diffusive motion. Simply subtracting the mean flow from particle trajectories and computing diffusivities does not give accurate results in this system [20].

In particular, for flow of the form $\vec{v} = \dot{\gamma} y \hat{x}$, i.e., uniform unbounded shear flow in two dimensions in which there is a constant shear rate $\dot{\gamma}$ creating a velocity gradient in the y direction, the second-order moments are given by Refs. [20,24]:

$$\langle yy \rangle = 2D_{yy}t, \tag{2}$$

$$\langle xy \rangle = 2D_{xy}t + D_{yy}\dot{\gamma}t^2, \tag{3}$$

$$\langle xx \rangle = 2D_{xx}t + 2D_{xy}\dot{\gamma}t^2 + \frac{2}{3}D_{yy}\dot{\gamma}^2 t^3. \tag{4}$$

These equations describe an ensemble average of particle positions $[x(t), y(t)]$ relative to the particle's initial location [i.e., [(x(0),y(0)]=(0,0)], without subtracting the mean flow.

These relations follow naturally for a PDF described by Brownian anisotropic diffusion with mean local flow $\vec{v}$ as above, and a diffusion tensor $\mathbf{D}$, with elements D_{xx}, D_{yy}, and $D_{xy} = D_{yx}$, where

$$\partial P/\partial t = \vec{v} \cdot \nabla P + \nabla \cdot D \nabla P. \tag{5}$$

Here, x corresponds to the streamwise direction and y is perpendicular to x. The left-hand sides of Eqs. (2)–(4) correspond to the y^2, xy, and x^2 moments of the probability density P.

The higher order terms in Eq. (4) are due to Taylor dispersion. For instance, the t^3 term arises because diffusive motion along $\pm\hat{y}$ moves grains to regions of different mean velocity $v(y)\hat{x}$ which tends to increase their separation or dispersion along the $\hat{x}$ direction. These higher order terms contribute to mean squared displacements which therefore appear superdiffusive.

It must be emphasized that Eqs. (2)–(4) are derived assuming that the diffusivities and shear rate are constant in space and time over an infinite plane. This condition is not met in the current experiment which changes the specific form of the correction terms.

Several issues concerning a diffusive picture must be addressed for sheared dense granular materials to determine whether Brownian diffusion applies. Two of these issues are the presence of a shear band and the limiting boundary at the shearing surface. Even assuming that a diffusive description is applicable, it remains to be determined on what temporal or spatial scales such a description should apply. In dense quasistatic flows, grains are generally close to a jammed state in which particles are in constant contact. Motion of grains requires the creation of voids, so correlated motion might be expected to be particularly important in dense 2D systems where paths are constrained. Short-lived vortex structures have been seen in 2D granular simulations [15] and experiments on 2D shearing of foams [25]. These are potential deviations from Brownian diffusive behavior which might affect the time evolution of the moments.

C. Previous measurements and simulations

The full diffusion tensor has been measured in granular gases using kinetic theory [17], simulations of rapid granular shear [18], and shearing of noncolloidal suspensions [26].

Substantial work on granular diffusivity in rapid flows has been done by Hsiau and co-workers who have measured self-diffusion coefficients in a variety of granular systems [11–13,27]. They find that fluctuations are anisotropic, with the largest fluctuations along the flow. Diffusivities are found to increase with shear rate and depend on the square root of the granular temperature T in agreement with kinetic gas theory. Other results in a similar chute flow were subsequently presented by Natarayan *et al.* [10].

Losert *et al.* studied a 3D fluidized Couette experiment [3], in which velocity fluctuations were found to be slightly larger in the direction along the mean flow. These fluctuations decrease roughly exponentially far from the inner cylinder, but decrease more slowly than the average velocity.

Radjai and Roux studied particle velocity fluctuations in numerical simulations under homogeneous strain in which there was no shear band formation [15]. They measured anomalous diffusion with an exponent of 0.9 (rather than 0.5 for ordinary diffusion) which they attributed to long-time configurational memory of a granular medium in quasistatic flows.

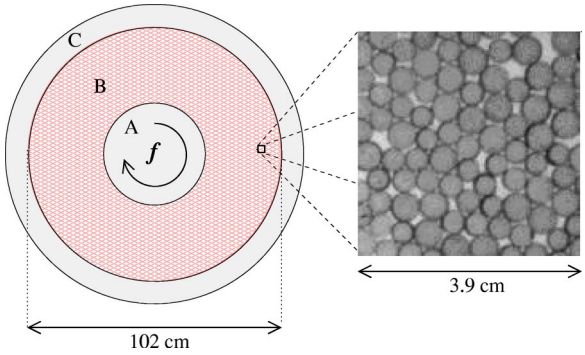

FIG. 1. Schematic of experiment as viewed from above. The granular material (b) is contained by the shearing wheel (a) and the outer ring (c). Their radii are $R_i = 20.5$ cm and $R_o = 51$ cm, respectively. On the right is a section of an experimental image of the grains.

Diffusivities have also been measured in a 3D rotating tumbler [6,7], 2D swirling flow [28], chute flow [9], simulations of shaken spheres [4], and simulations of small numbers of spheres in suspension [29]. Earlier studies primarily addressed rapid flows from kinetic theory [16].

Although these studies are relevant here, we note that the displacements were assumed to be purely induced by the shear flow and no attempt was made to investigate the role of the force chain network.

D. Organization of presentation

The paper is organized as follows. In Sec. II, we describe the experimental techniques. We present diffusion measurements in Sec. III and results from a random walk simulation in Sec. IV. We show the impact of the anisotropic force network in Sec. V. We discuss diffusivities determined from the velocity autocorrelation functions in Sec. VI. In Sec. VII, we show examples of intermittent vortices and Lévy flight trajectories, and in Sec. VIII, we draw conclusions.

II. EXPERIMENTAL TECHNIQUES

The experiment is performed with a 2D Couette apparatus, as sketched in a top view in Fig. 1. The granular material (B) consists of a bidisperse mixture of about 40 000 disks (diameters $d_S = 0.42$ cm, $d_L = 0.50$ cm, thickness $= 0.32$ cm) in a ratio of 3 small:1 large. The bidisperse mixture is used to inhibit crystalline ordering of the disks. The disks lie flat on a Plexiglas sheet bounded by an outer ring ($R_o \equiv 51$ cm) (C) and an inner shearing wheel ($R_i \equiv 20.5$ cm) (A). A Plexiglas sheet covers the experiment to protect the experiment from external perturbations, but the sheet does not contact the particles. The shearing wheel is rotated at a frequency f of 0.1–10.0 mHz or a speed of $v \approx 0.013$–1.3 cm/s at the shearing surface. The experiment is initially run for at least one revolution of the shearing wheel in order to avoid effects from transients, an issue that will be addressed in another paper [30]. The shearing wheel and the outer ring have teeth with gaps comparable to the size of the smaller particles.

The system is lit from below and observed from above using a 2 megapixel charge-coupled device (CCD) camera at a frame rate of up to 7.5 Hz. Sequences of approximately 1500 images are analyzed to determine particle trajectories. Disks within about 20 particles diameters of the shearing wheel are marked with lines, thus allowing us to track particle position and orientation and to identify particles by size. Approximately 4000 grains are typically in the field of view, of which 2500 are marked. Images are thresholded and the orientation and position of lines on the disks are found. Sufficient temporal resolution is used such that each particle in a frame can be connected with the closest grain in the subsequent frame to establish particle trajectories.

The force network can also be visualized since the grains are made of a photoelastic material [31]. When polarized light travels through the disks, it experiences a phase shift (birefringence) proportional to the difference in principle stresses $\sigma_2 - \sigma_1$. When the disks are illuminated between crossed polarizers, grains under larger stress are seen as regions of larger gradients in light intensity. In this way, the force network is visualized as a network of bright lines on a dark background. Additional details were presented by Howell *et al.* [1]. The polarizers are removed for measuring particle trajectories and diffusivities.

III. DIFFUSION MEASUREMENTS

A. Mean velocity profiles

We first consider the mean properties of the flow. In Fig. 2, we show the mean tangential velocity v_θ versus radial distance from the shearing surface, $r \equiv R - R_i$, where R is the distance from the center of the shearing wheel. The velocities are scaled by the velocity of the shearing surface $V_0 = 0.28d/\mathrm{s}$ where d is the mean particle diameter $[d = (d_S + d_L)/2]$. For this particular run, we used a frame rate of 1.08 Hz, so that the shearing wheel was displaced $0.25d$ between each of the 1080 images, which, in total, correspond to one revolution of the shearing wheel. The limiting value for v_θ of approximately 10^{-4} corresponds to the sensitivity of the measurement for a typical number of images and spatial resolution, e.g., for an image resolution of 20 pixels per diameter, a grain displacement of $\frac{1}{20}$ pixel over the entire run would give a mean velocity $\overline{v_\theta} = \frac{1}{1080}(d/20)1.08\ \mathrm{Hz} = 5 \times 10^{-5}(d/s)$ (or $v/V_0 \approx 10^{-4}$) and velocities smaller than this cannot be resolved. Motivated by previous results for Couette shear [2,32], we fit the data ($r < 7.5d$) to an exponential $[v_\theta(r) = 1.071 \exp(-0.521r)]$ and to a Gaussian $[v_\theta(r) = 0.925 \exp(-0.284r - 0.0534r^2)]$.

From this individual run, the Gaussian fit seems most appropriate. However, this is an artifact of the data resolution. Additional data with slower frame rates point to an important issue concerning particle tracking velocimetry. If the number of images N remains fixed, by taking data using slower frame rates, velocities of slower particles further from the shearing surface can be accurately measured while faster particles at the shearing surface can no longer be accurately tracked. We show these results in Fig. 3 in which the frame rate $(\equiv 1/\Delta t)$ is varied for different runs at the same imposed shear rate ($f = 1$ mHz, $N = 1500$). The individual curves are

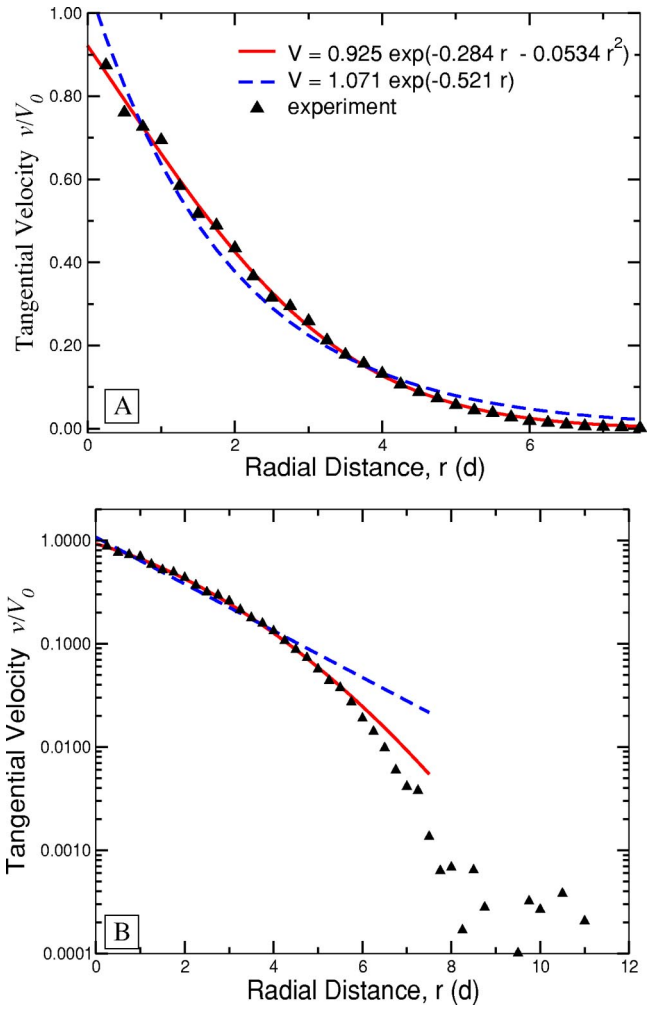

FIG. 2. Mean tangential velocity vs radial distance from the shearing surface plotted on a (a) linear and (b) logarithmic scale for a particular run. The velocity v is scaled by the velocity of the shearing surface V_0. The experimental data ($\triangle, r<7.5d$) is fitted to an exponential (dashed line) and a Gaussian (solid line). $f=1$ mHz and $V_0=0.28d/\mathrm{s}$.

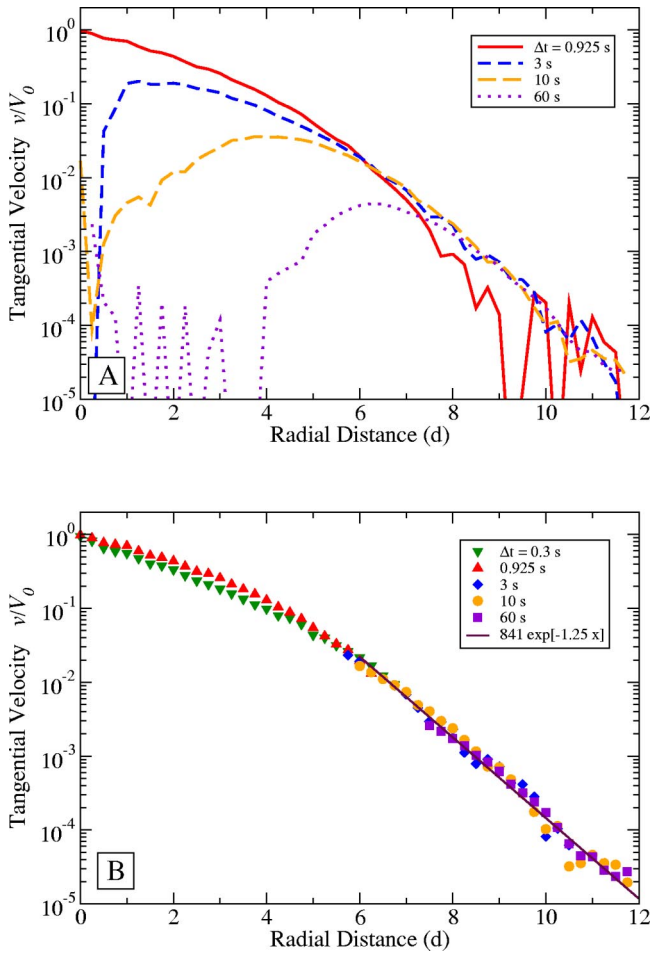

FIG. 3. (a) Tangential velocity vs radial distance from the shearing surface using experimental runs at different frame rates ($\equiv[1/\Delta t]$) as described in text. Velocities v are shown relative to the velocity of the shearing surface $V_0=0.28d/\mathrm{s}$. (b) Data is shown where velocities can be resolved given the frame rate and number of pictures. An exponential tail is observed in which $v_\theta \propto e^{-1.25r}$.

accurate over a particular range of velocities based on the frame rate and number of pictures in the run. In Fig. 3(b), we show data for each set within this range. It becomes evident that the velocity profile has an exponential tail which is obscured when simply analyzing a single run. Previous results have shown exponential [1,19], Gaussian [2], and similar strongly decaying [3] velocity profiles for Couette flow. Authors of these studies [1,2] have suggested that the differences in measured profiles may depend on whether the flow is 2D or 3D or on whether the particles are rough or smooth. The present data suggest that an additional factor may be spatiotemporal resolution. Particle tracking issues in particular have been addressed recently by Xu *et al.* [33].

We conclude that correct tracking occurs for velocities that approximately satisfy

$$\frac{1}{N}\frac{1}{20}\frac{d}{\Delta t} \lesssim \overline{v}_\theta \lesssim 0.1\frac{d}{\Delta t}, \tag{6}$$

where N represents number of pictures, and the image resolution is 20 pixels per diameter d. The lower speed limit is set by image and temporal resolution. The upper limit is chosen to resolve the occasionally fast displacements well above the mean. Note, however, that the upper cutoff is not an issue when the speed of the shearing surface is less than $d/\Delta t$, since generally, all particle displacements can be resolved, e.g., for $\Delta t=0.3$ s and 0.925 s, the requirement that $\overline{v}_\theta < 0.1(d/\Delta t)$ is not necessary.

B. Radial and tangential diffusivities, D_{rr} and $D_{\theta\theta}$

We measure diffusivities by tracking individual particles, and hence their displacements, over time in both the radial ($\hat{r}$) and tangential ($\hat{\theta}$) directions. We subtract the mean flow (Fig. 2) from the tangential velocity component at each time step.

Although Eqs. (2)–(4) characterize absolute x and y displacements without subtracting the mean flow, they are also predicated on a velocity profile such that $\langle x(t)\rangle = \langle y(t)\rangle$

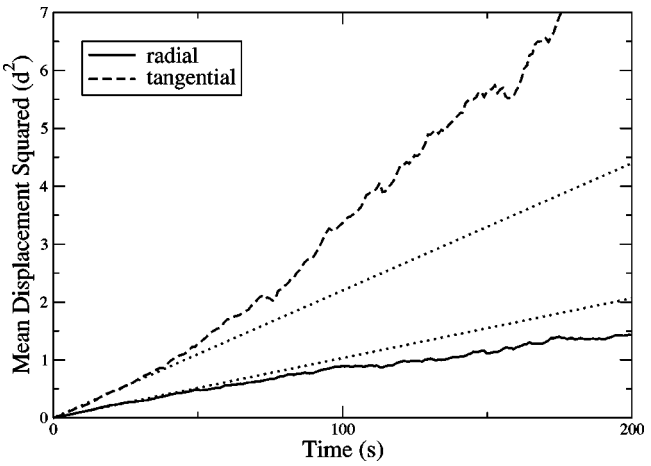

FIG. 4. Mean displacement squared vs time for tangential and radial directions for particle trajectories starting at $2d<r<3d$ and shearing wheel frequency of $f=1$ mHz. Dotted lines show linear fits to $t<30$ s.

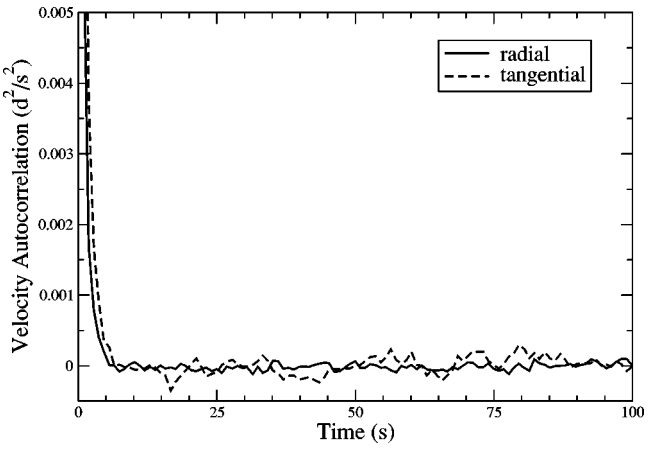

FIG. 5. Velocity autocorrelation vs time for particles in $2d<r<3d$ for radial and tangential velocity components.

$=0$ which is true for a uniform shear rate in an infinite domain, neither of which are true here. The exponential velocity profile observed in the experiment invalidates this and prevents us from directly comparing to Eqs. (2)–(4). Deriving the corresponding moment evolution equations with the exponential profile of the velocity and diffusion fields is significantly more complicated and beyond the scope of this paper. Instead, we use a random walk model in Sec. IV to model the system. Nonetheless, the theory above explains the origin of the Taylor dispersion effects that we observe. In order to avoid the effects of a mean displacement due to the locally varying shear rate, we remove the mean flow. The resulting mean displacement squared is plotted versus time and averaged for different particles initially within the same radial bin (bin size $=d$ or $d/2$). An initially linear evolution indicates ordinary diffusive behavior with the slope of the line equal to $2D$.

Figure 4 shows a typical example of the mean displacement squared for the tangential $\langle (R\Delta\theta)^2 \rangle$ and radial $\langle (\Delta r)^2 \rangle$ directions for particles in the shear band. Here, the Δ notation reminds us that the mean flow is subtracted from the data. The dotted lines are linear fits for $t<30$ s giving diffusivities proportional to the slopes. The tangential diffusivity is approximately double the radial diffusivity at small times. The former is expected to deviate from a straight line due to the higher order terms similar to those in Eq. (4). Note, however, that for small t, the linear term in Eq. (4) dominates, and Taylor dispersion effects are not present.

One might worry that using early times would be inaccurate when diffusivity is generally defined as a long-time behavior. In particular, results for more rapid flows show an initial ballistic regime [5,9,18], and significant velocity autocorrelations appear in noncolloidal suspensions [20]. However, in the quasistatic motion of the present experiment, there is no ballistic behavior because grains are constantly in contact with each other. Moreover, as seen in the velocity autocorrelation shown in Fig. 5, the velocities quickly become uncorrelated. The time for the correlation to reach zero corresponds to a mean relative grain displacement of $0.25d$ and occurs within 4 s for this data. Therefore, diffusivities measured for 5 s$<t<30$ s can be expected to be beyond the correlated regime and are at times before significant Taylor dispersion effects are observed. We show below, using a random walk simulation, that the apparent subdiffusivity of the radial component in Fig. 4 is due to the radial gradient in shear rate, an effect that is not included in Eqs. (2)–(4) above.

Figure 6 shows $\langle (R\Delta\theta)^2 \rangle$ and $\langle (\Delta r)^2 \rangle$ for particles initially at various distances from the shearing surface. It is evident that the diffusivity is larger close to the shearing surface, i.e., in regions of large shear, as observed previously. In addition, the maximum diffusivity occurs at $r\approx 2d$. The fact that the maximum diffusivity does not occur at $r=0$ is due to nondiffusive motion of particles in contact with the shearing wheel. Since most of these particles ($r<2d$) are dragged by the wheel at the same speed and the mean velocity has been subtracted, the fluctuations are smaller. In Fig. 7, we show the rms displacements versus time on a log-log scale. The solid line shows the expected slope for diffusive behavior.

As seen in Fig. 8, the diffusivity is proportional to the local shear rate $\dot{\gamma}$. For this figure, we use the local shear rate determined from the slope of Fig. 2, and a diffusivity that is half the slope of Δr^2 versus t for $t<30$ s. The decrease in diffusivity at large shearing rate (i.e., close to the shearing surface) is due to particles being dragged by the shearing wheel and hence exhibiting ballistic behavior. For the radial and tangential directions, $D\approx 0.1-0.2\ d^2\dot{\gamma}\approx 0.4-0.8a^2\dot{\gamma}$, where a is the particle radius, i.e., the scale of the diffusivity is approximately given by $a^2\dot{\gamma}$. As a consequence of the exponential tail of the velocity profile, the diffusivity also decays roughly exponentially, such that the diffusive motion is effectively confined to the shear band.

Figure 9(a) shows results for diffusivity versus local shear rate ($r>2d$) for three different rotation frequencies of the shearing wheel. The diffusivity is approximately proportional to local shear rate over a large range of shearing rates from separate experimental runs, and $D_{\theta\theta}/D_{rr}\approx 2$. In Fig. 9(b), the diffusivity at each data point was divided by the local

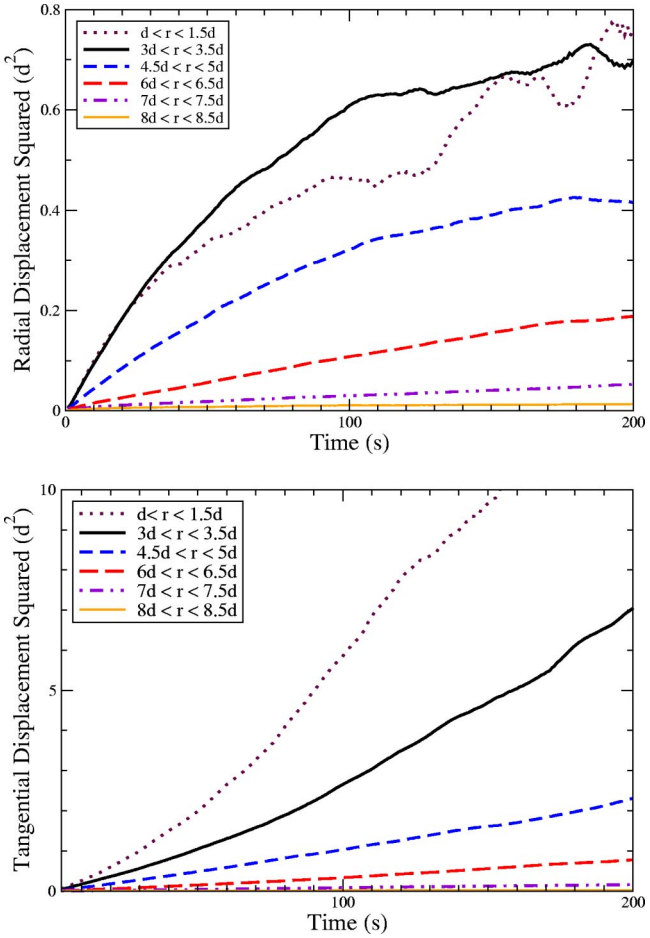

FIG. 6. Mean displacement squared vs time at different distances from shearing wheel. Radial displacements shown on top and tangential displacements on bottom. $f=1$ mHz.

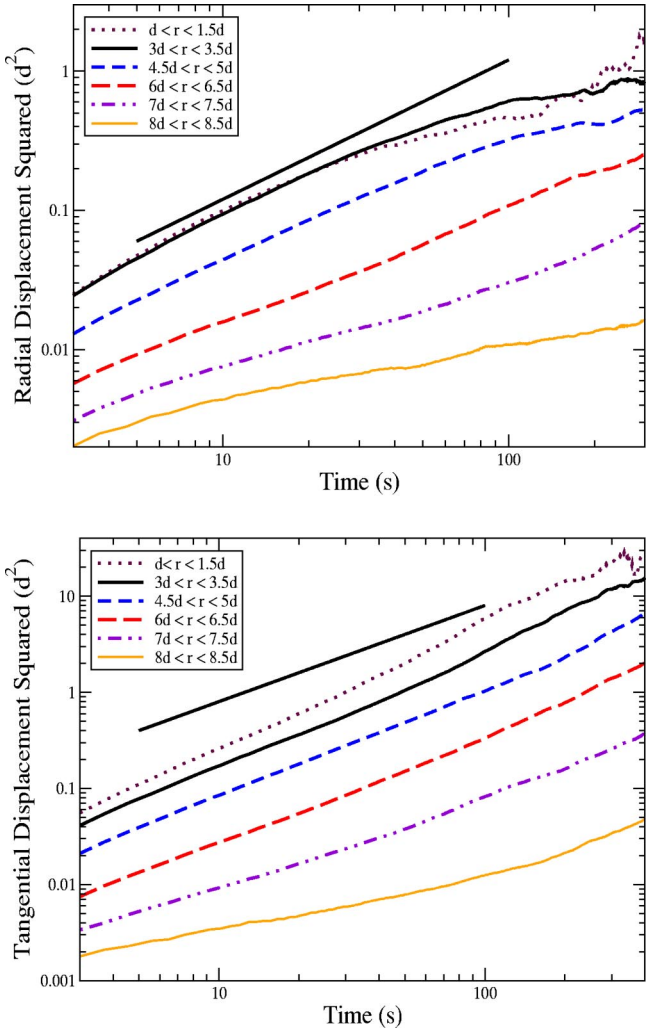

FIG. 7. Log-log plot of displacement squared vs time for data in Fig. 6. Radial displacements given in plot on top and tangential displacements on bottom. The straight solid line gives the expected behavior for diffusive motion.

shear rate. The resulting data $(D/\dot{\gamma})$ are roughly constant over 3 orders of magnitude of shear rate. The lines show fits for tangential diffusivities $D_{\theta\theta}=0.223\dot{\gamma}$ and radial diffusivities $D_{rr}=0.108\dot{\gamma}$. The data for $D_{\theta\theta}$ are noisier than that for D_{rr} since due to the mean flow the magnitude of the tangential motion is much larger than radial motion.

C. Off-diagonal diffusivity $D_{r\theta}$

The off-diagonal diffusion constant $D_{r\theta}$ is shown in Fig. 10. This diffusion coefficient is an order of magnitude smaller than D_{rr} and $D_{\theta\theta}$. Away from the shearing surface, $D_{r\theta}$ is also negative. This is due to the anisotropic force network and will be addressed below.

IV. RANDOM WALK SIMULATION

As mentioned earlier, direct comparison of the data to Eqs. (2)–(4) is not possible. The fact that $v(r)$ and $D(r)$ decay exponentially and the presence of the boundary at $r=0$ in the experiment are inconsistent with the assumptions leading to the moment evolution equations in Sec. I B. An exact solution of the moment equations with the appropriate boundary conditions and spatial dependence of $D(r)$ and $\vec{v}(r)$ is difficult. However, a numerical simulation with appropriate spatial dependence in D and $\vec{v}$ using a random walk model is relatively simple.

In this section, we present such a simulation in which we assume diffusive motion and impose an exponential velocity profile and impenetrable inner boundary so as to parallel the experiment. To model radial diffusion, a walker makes a step each time τ with equal probability along $\pm\hat{r}$ with a radial step length $L_r(r)$ proportional to $[\dot{\gamma}(r)]^{1/2}$, where $\dot{\gamma}$ is the experimentally measured shear rate. That is, $L_r(r)=c_1[\dot{\gamma}(r)]^{1/2}$, where c_1 is a constant. This imposes a diffusivity $D\propto L(r)^2/\tau\propto\dot{\gamma}(r)$ in agreement with Fig. 9. Radial motion is bounded by the shearing wheel, so any step that would move a particle through that boundary is automatically forced to be a step away from the shearing wheel (i.e., towards positive r). Tangential motion is modeled in a similar way. At each time step, the walker is advected at the experimentally measured mean velocity based on its radial position (Fig. 2) and also randomly takes an additional step

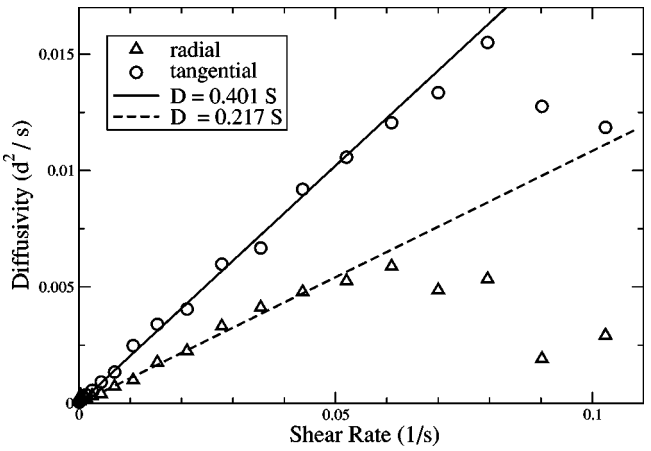

FIG. 8. Diffusivities D vs local shear rate $\dot{\gamma}(f=1$ mHz). Diffusivities are proportional to the local shear rate. Close to the shearing wheel, at larger shear rates, the diffusivity decreases because particles at $r<2$ are typically dragged continuously by the shearing wheel. The solid line shows $D=0.200\dot{\gamma}$ and the dashed line shows $D=0.108\dot{\gamma}$.

along $\pm\hat{\theta}$ with tangential step length $L_\theta(r)=c_2\dot{\gamma}(r)^{1/2}$. This model contains two free parameters c_1 and c_2, corresponding to the magnitude of D_{rr} and $D_{\theta\theta}$. Equivalently, the fit parameters can be thought of as determining an overall scale factor for the data and the ratio of radial to tangential diffusivities. Here, we do not consider additional anisotropies associated with the force chain network.

Figure 11 shows a mean-square displacement versus time for the simulated data. The experimental data from Fig. 6 is also included for reference as thin solid lines. The simulation is performed assuming $D_\theta/D_r=1.9$ $(c_1=0.48,\ c_2=0.66)$. As noted, the two free parameters set the scale of the radial and tangential displacements. We emphasize that the relative magnitudes of the data at different distances from the shearing wheel and the apparent subdiffusive and superdiffusive behavior at longer times result from the experimentally measured velocity profile.

Although the initial slope of the lines in Fig. 11 is equal to $2D(r)$, the long-time behavior and deviation from a straight line is due to the coupling to the mean flow. The horizontal and vertical scales of Figs. 6 and 11 are identical in order to compare the long-time behavior. This confirms that the apparent subdiffusion and superdiffusion is due to the mean flow.

In particular, it is clear that the curvature of the D_{rr} data for particles close to the shearing surface, which appeared to be subdiffusive, arises from the gradient in local shear rate. That is, the grains next to the wall diffuse away to a region of slower shearing rate and, once away from the wall, diffuse more slowly. If this gradient is removed from the simulation (i.e., $\dot{\gamma}$ is assumed constant), the lines become straight with approximately the same slope. The presence of a wall ($r=0$) also tends to decrease the diffusivity at small r, but this is a much less pronounced effect than that of the gradient in shear rate. Note in Fig. 11 that simulated grains close to the shearing wheel show an apparent superdiffusive behavior due to Taylor dispersion.

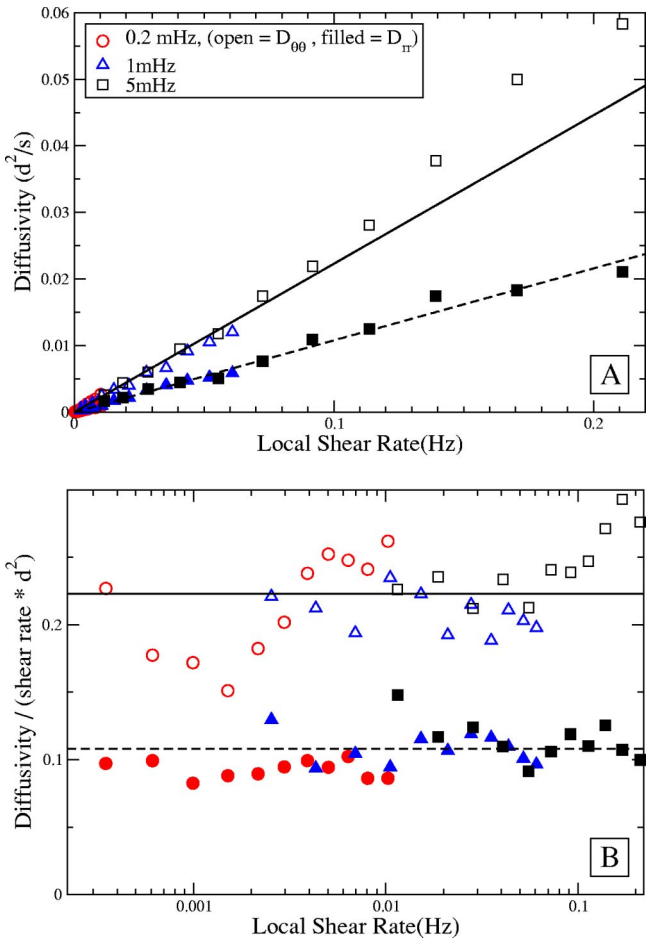

FIG. 9. (a) Diffusivities vs local shear rate for grains at $r>2$ for three different rotation rates of the shearing wheel. In (b), the diffusivities are rescaled by the local shear rate $\dot{\gamma}$ and d^2. The lines show fits for $D_{\theta\theta}=0.223\dot{\gamma}$ (solid) and $D_{rr}=0.108\dot{\gamma}$ (dashed) which approximately hold for 3 orders of magnitude of shear rate.

We note that in the experiment, grains at $r<2$ are generally dragged by the shearing wheel which tends to decrease

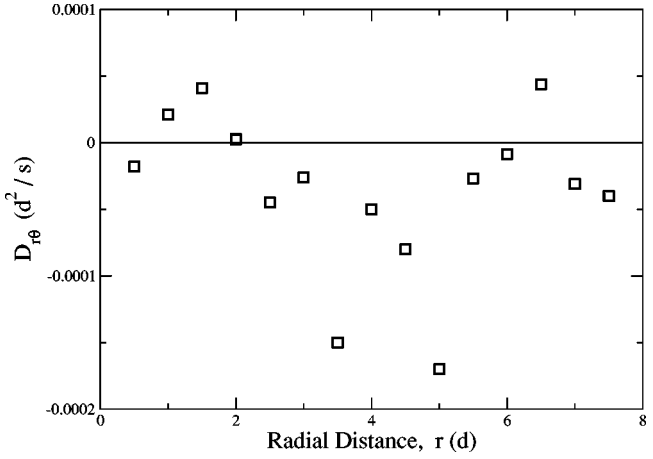

FIG. 10. Off-diagonal diffusivity $D_{r\theta}$.

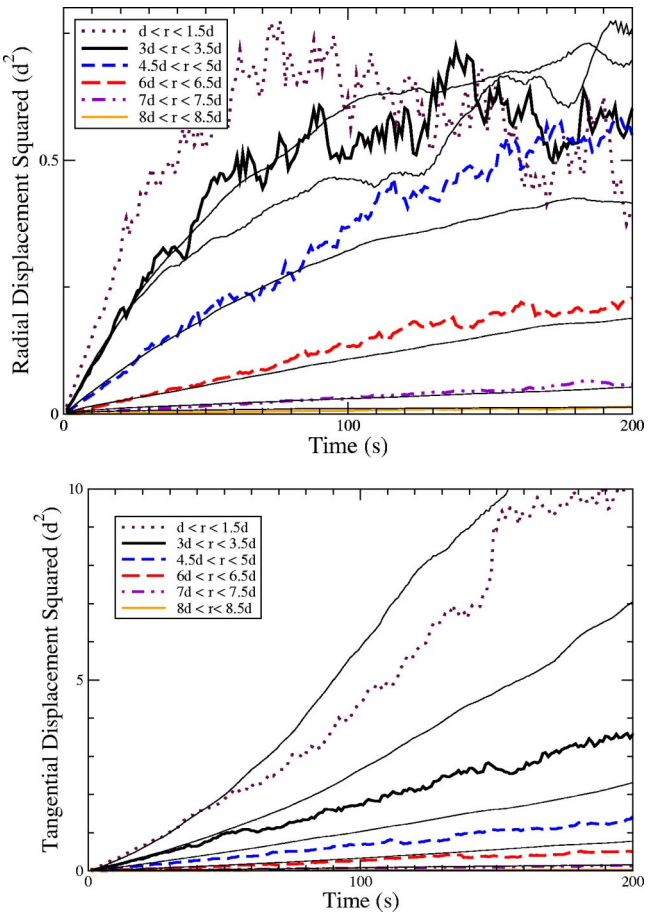

FIG. 11. Mean displacement squared vs time for simulation of random walk in which the experimentally measured velocity profile is imposed. Radial displacements shown on top and tangential on bottom. The thin solid lines show the experimental data from Fig. 6.

the apparent radial diffusivity and add to the effects of Taylor dispersion (which accounts for the slight difference in the magnitudes of Figs. 6 and 11). However, Fig. 11 reveals that the dominant effects are the shear gradient and Taylor dispersion. Thus, the main features of the apparent subdiffusive and superdiffusive behavior are observed even though the simulation does not include the effect of ballistic motion due to dragging of particles by the shearing wheel.

We show the measured diffusivities for the experiment and the random walk simulation together in Fig. 12. There is very good agreement except for $r<2$, where the simulation overestimates the diffusivity.

V. EFFECTS DUE TO ANISOTROPIC FORCE NETWORK

In the previous discussion, we tacitly assumed that the natural coordinate system for diffusion measurements is set by the radial and tangential directions, corresponding to the anisotropy of the imposed shear. However, dense systems, unlike dilute rapid flows, have anisotropic force networks due to imposed shear which are in general at a different orientation from the flow direction. This is seen by using the photoelasticity of the grains to image the force chains, as in Fig. 13(a). This figure shows a typical case where the force

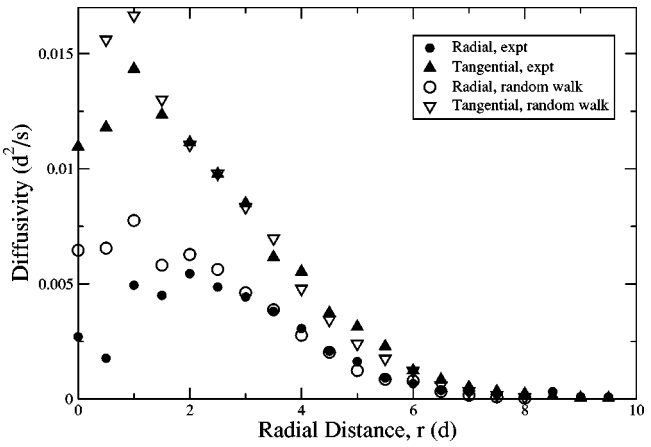

FIG. 12. Diffusivity vs radial distance from the shearing surface for experimental data and the random walker model. The deviation between simulation and experiment for $r<2$ is due to particles being dragged nondiffusively by the shearing wheel.

chains are preferentially oriented to oppose the motion of the shearing wheel, at an angle that is intermediate between the $\hat{r}$ and $\hat{\theta}$ directions. We might expect the diffusivity to be affected by the anisotropic force network. To determine this angle, images such as Fig. 13(a) can be transformed from polar to Cartesian coordinates, such that the shearing wheel is located at $y=0$ [Fig. 13(b)]. In this figure, each vertical line corresponds to a radial line in the original image. Since the curvature of the wheel is relatively small, the transformation is not dramatic and distortion of the image is small. A 2D autocorrelation of image 13(b), then provides a measure of the mean force chain orientation [13(c)]. The mean angle ϕ of the force chains fluctuates strongly in time around a mean value of 20°–30° relative to $\hat{r}$.

To determine the angular dependence of the diffusive motion, we locally project displacements at each time step onto an axis rotated at an angle ϕ from the radial direction, as sketched in Fig. 14. That is, for each step, the displacement is locally parametrized in terms of radial and tangential com-

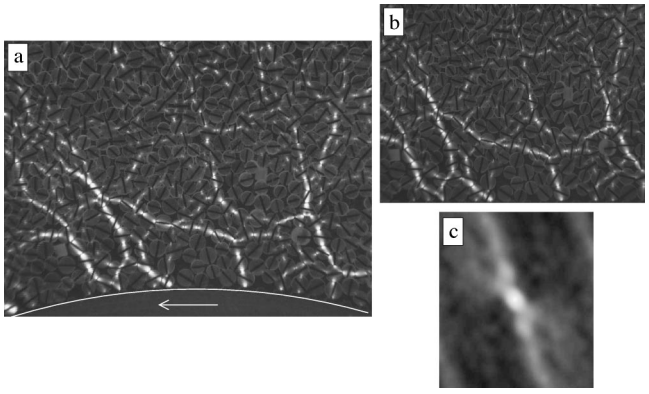

FIG. 13. (a) Force chains imaged using photoelastic grains. The shearing wheel is marked by the white line and is rotating to the left. (b) Image (a) is rescaled from polar to Cartesian coordinates such that the shearing wheel is at $y=0$. (c) A 2D autocorrelation of (b) which characterizes the orientation of the strong force network.

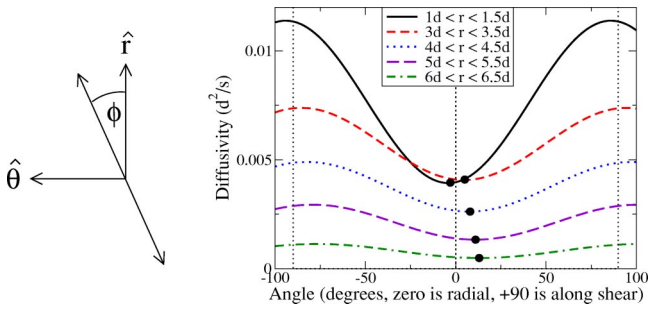

FIG. 14. We locally project displacements at each time onto an axis rotated at an arbitrary angle ϕ degrees from the radial direction. $D_{\phi\phi}$ is measured vs ϕ and plotted with the minimum diffusivity indicated by the filled circles.

ponents (relative to the center of the shearing wheel) and then are locally projected onto an axis rotated by ϕ relative to the r direction. We then use the ϕ components of the trajectories to measure a diffusivity $D_{\phi\phi}$ along this direction. On the right side of Fig. 14, we show $D_{\phi\phi}$ versus ϕ for grains at different radial distance r. Again, the diffusivities decrease with distance from the shearing wheel. In addition, the direction of minimum diffusivity ϕ_{min}, marked by the solid circles, changes with distance from the shearing wheel.

In Fig. 15, we show the angle of minimum diffusivity ϕ_{min} versus distance from the shearing wheel which we determine by fitting a parabola to $D_{\phi\phi}$ in the region $\phi_{min} \pm 30°$. Close to the shearing surface, at high shear rates, the minimum diffusivity is in the radial direction, corresponding to the minimum expected based on the imposed shear direction. At larger distances r, the minimum shifts towards the direction of the mean force chain orientation. In other words, outside of the immediate vicinity of the shearing wheel, the anisotropic force network affects particle motion and must be taken into account in order to properly describe the diffusive motion in dense granular systems.

We use the same procedure for deducing the angular dependence of the diffusivity on a number of independent data

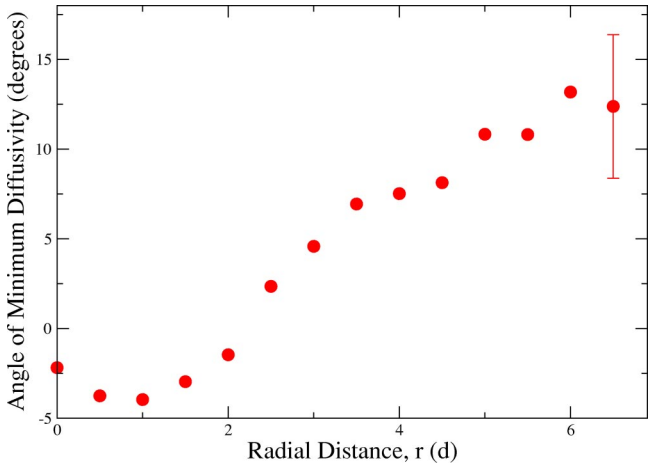

FIG. 15. The angle ϕ corresponding to the minimum diffusivity ϕ_{min} is measured from Fig. 14. The increase with radial distance corresponds to the minimum diffusivity becoming more aligned with the mean direction of force chains.

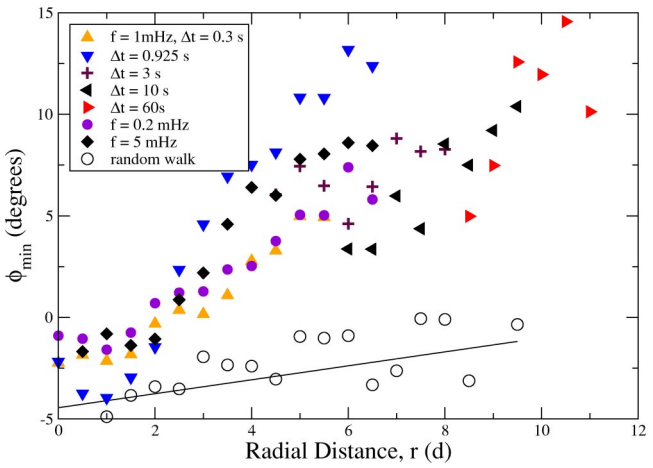

FIG. 16. The angle of minimum diffusivity ϕ_{min} vs r measured according to Fig. 14 for multiple data sets. Again, the orientation of minimum diffusivity shifts towards a direction that corresponds to the mean force chain direction. The same analysis is performed on the random walk data (○ and linear fit) which does not model the anisotropic force network.

sets, including the data used to create the velocity profile of Fig. 3 and on two additional data sets with different shearing rates. We show data in Fig. 16 only for velocities that are properly resolved, as in Fig. 3. Although there is some significant variability from one data set to the next, there is a clear trend in which ϕ_{min} shifts towards the direction of force chain orientation as r increases. When we perform the same analysis on the simulated data, in which there is no force network, ϕ_{min} does not increase above 0° as indicated by the open circles. The fact that these points are negative is addressed in the following section.

VI. DIFFUSIVITY AND VELOCITY AUTOCORRELATION FUNCTIONS

Diffusivities (D_{rr} and $D_{\theta\theta}$) can also be determined using velocity autocorrelations from the expression

$$D_{xx} = \int_0^\infty \langle v_x(t) v_x(t+\tau) \rangle d\tau, \tag{7}$$

where the velocity at each time step is simply defined as $v_x(t) \equiv [x(t) - x(t-1)]/\Delta t$. The integral must be taken over times long enough to extend beyond the initial correlated region. Thus, for this data,

$$D_{xx} = \Delta t \sum_{dt=0}^{N} \langle v_x(t) v_x(t+dt) \rangle, \tag{8}$$

where we use a cumulative sum of the autocorrelation (Fig. 5). After an initial transient of about 5 s, the curve fluctuates around a constant value. The average of the data well after the transient (85–185 s, for this data set) is taken as the diffusivity. Figure 17 shows the diffusivities determined from the velocity correlations. For the most part, they agree quite well with diffusivities determined from the displacement squared versus time data which are indicated by lines

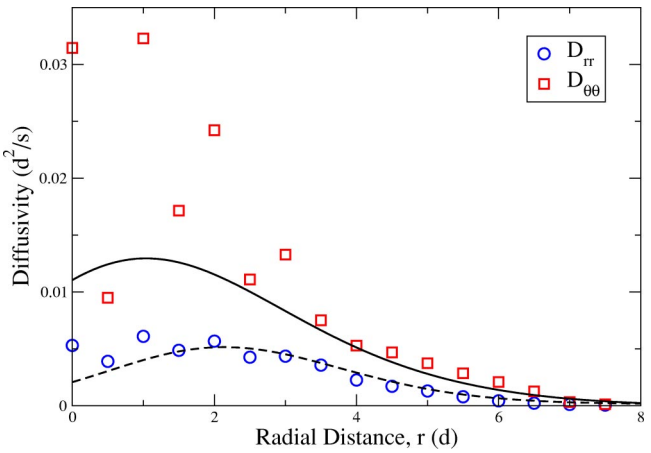

FIG. 17. Diffusivities determined from velocity autocorrelations using Eq. (7). The shearing wheel frequency is $f=1$ mHz. The lines show fits to the tangential (solid) and radial (dashed) diffusivities in Fig. 12 for comparison.

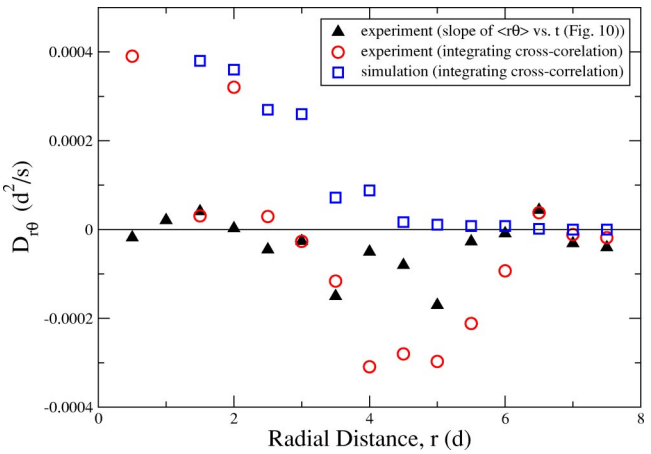

FIG. 18. Off-diagonal diffusivity determined by integrating the velocity cross correlation. Data determined from the slope of displacement squared vs time plots (Fig. 10) is shown for comparison. $D_{r\theta}$ for the random walk simulation is also shown.

showing fits to the data of Fig. 12. The exception is for tangential diffusivities of particles adjacent to the shearing wheel. This discrepancy is due to the fact that there is some non-negligible correlation in the tangential velocity after $t=30$ s for particles in contact with the shearing wheel.

The off-diagonal diffusivity must be determined using [34]

$$D_{ij}=\frac{1}{2}\int_0^t (\langle v_i(t')v_j(t)\rangle+\langle v_i(t)v_j(t')\rangle)dt', \qquad (9)$$

which for large t can be rewritten as [18]

$$D_{ij}=\frac{1}{2}\int_{-\infty}^{\infty}\langle v_i(t)v_j(t+\tau)\rangle d\tau, \qquad (10)$$

assuming the motion is statistically stationary over time. This reduces to Eq. (7) for the diagonal terms, $i=j$. The off-diagonal diffusivity, $D_{r\theta}$ is shown in Fig. 18 along with data determined using the displacement squared versus time plots (Fig. 10). Since the magnitude of $D_{r\theta}$ is small, the fluctuations lead to larger noise in these results.

Further from the wheel, where the minimum diffusivity shifts to larger angles, the cross-correlation term is negative. This indicates that motion along $\hat{\theta}$ is anticorrelated with motion along $\hat{r}$, which agrees with a decrease in diffusivity along positive ϕ, and a shift in minimum diffusion angle towards positive ϕ. To emphasize the effect of the anisotropic force network, we contrast the experimental results with data from the simulation, where there is no force network effect and $D_{r\theta}$ is always positive (Fig. 18).

The fact that $D_{r\theta}$ is positive in the simulation is due to the velocity gradient, an effect that was also observed in previous measurements of the cross term (typically designated as D_{xy}) [17,18,26]. Note that a positive $D_{r\theta}$ in the present data corresponds to a negative D_{xy} in previous results. This difference in sign is due to the fact that the authors of Refs. [17,18,26] used the convention that v_x increases with y. By contrast, we have chosen the natural experimental coordinate system $y\equiv r$ such that $y=0$ at the boundary (shearing wheel) and increases into the bulk, i.e., v_x decreases with y.

Returning to the present studies, the fact that $D_{r\theta}$ is positive for the simulation is the origin of the slightly negative ϕ_{min} seen in Fig. 16. We emphasize that the positive ϕ_{min} and negative $D_{r\theta}$ in the experimental data have the opposite sign from the simulation. This difference in sign is due to the presence of the strong force network in the experiments, an effect that is absent in the simulations.

VII. LÉVY FLIGHTS AND VORTICES

We also observe examples of correlated motion and trajectories similar to Lévy flights [35] which could contribute to nondiffusive motion. In fact, the dense 2D packing leads to caging and coordinated motion such that neighboring grains tend to move together. This differs from more dilated flows in which collisions are the source of fluctuating motion. The fact that the present system behaves diffusively on average indicates that long-range correlated motion is sufficiently rare and random over time that the mean behavior is not affected.

It is interesting to ask whether such novel behavior as Lévy flights occur in our system and whether they are important. Lévy flights are random walks in which occasional large steps, or flights, are observed, such that apparent Brownian motion on smaller scales is punctuated by large displacements. They also have the property that the variance of the step size $\langle L^2\rangle$ and therefore the diffusivity ($\propto L^2/\tau$) are infinite. This situation can be realized if the probability of the walker making a step L is given by a power law $P(L)\propto L^{-\alpha}$, where $2<\alpha<3$. This is in contrast with Gaussian or exponential distributions of L in which case large steps are much more rare and the variance is finite.

In Fig. 19(a), we show trajectories for particles in the shear band. Each line shows the trajectory of a single particle over the same time period (1000 s). Next to the shearing surface (bottom of image), particles travel relatively fast

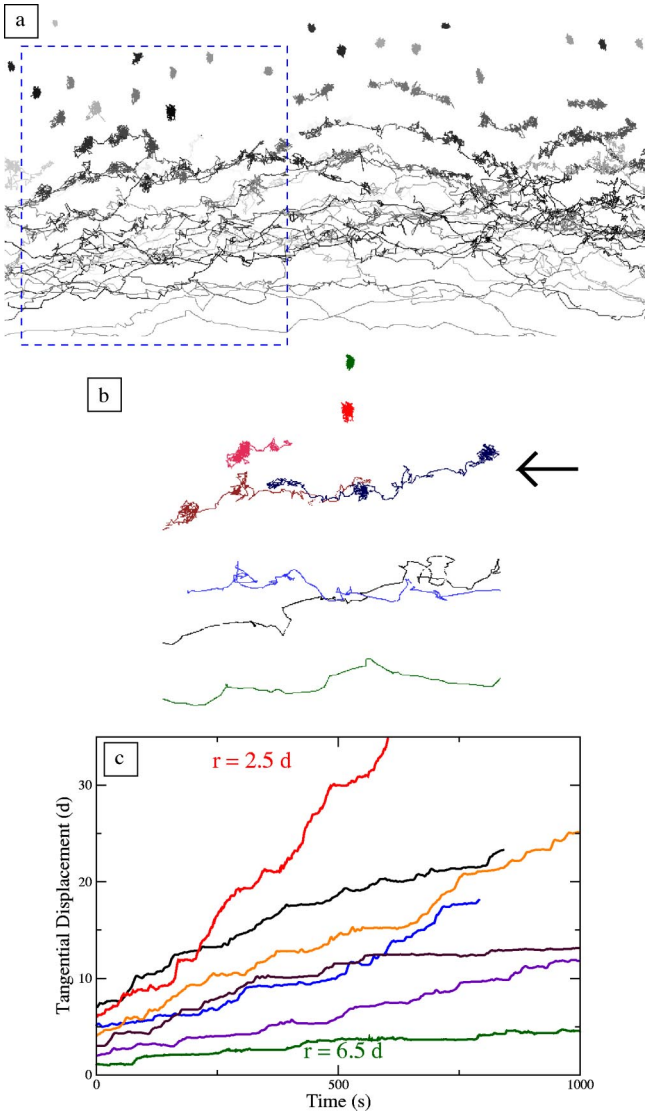

FIG. 19. (a) Trajectories in the shear band are shown for a fixed time (1000 s). (b) A few individual trajectories from the dashed box in (a) are shown. Motion similar to Lévy flights is occasionally observed ($r \approx 4-5d$), in the region indicated by the arrow. Small fluctuations of particle position are observed with occasional larger scale advection. (c) Tangential displacements vs time for seven individual trajectories ($r \approx 2.5d, 3d, 3.5d, 4d, 4.5d, 5.5d, 6.5d$) chosen to highlight Lévy-like motion. Trajectories closer to the shearing wheel are displaced upwards at $t=0$ for clarity.

compared to particles outside of the shear band (top of image), which fluctuate around effectively stationary positions. Figure 19(b) shows a few particular trajectories from the dashed region of Fig. 19(a). At the edge of this band ($r \approx 4-5d$), we see trajectories that are reminiscent of Lévy flights, in which relatively large displacements occur between periods of fluctuating motion on a smaller scale. To observe this better, in Fig. 19(c), we plot tangential displacement versus time for seven trajectories at different distances from the shearing wheel. The data have been smoothed over a 5 s running window. We note that these are not necessarily typical trajectories, but have been chosen to elucidate the

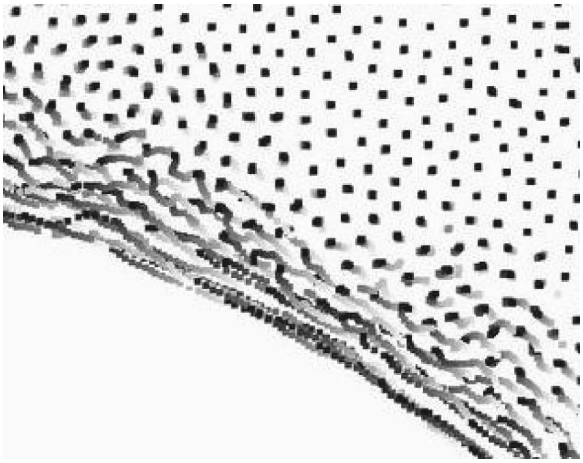

FIG. 20. Granular vortices (upper left) are occasionally observed in plots of particle trajectories over 25 s. Particle position is indicated by a dot with darker gray scale levels used for later times.

presence of Lévy-like behavior. In this plot, regions of small fluctuations (nearly flat lines) are separated by faster jumps along the mean flow direction.

These data can be compared with an example from a rotating flow fluid experiment ([36] e.g., Fig. 7) from which similar data were obtained. Although we observe somewhat similar motion, the trajectories in Fig. 19 have a different origin. In the fluid case, particles exhibit flights between periods in which they are trapped by vortices. In the granular system, grains become trapped as they move farther from the shearing surface and remain effectively trapped until they move closer to the wheel. In addition, it is common for local rearrangements involving 10–20 grains to occur intermittently. (A similar effect may also account for the Lévy distributions of trapping times for observations of grains deposited on sand piles [37].) With the present data, e.g., Fig. 19, we do not have sufficient statistics to determine whether the trajectories exhibit Lévy scaling because flightlike trajectories are rare.

We also occasionally observe cooperative motion as in Fig. 20, which displays particle trajectories over a 25 s window in which the gray scale level indicates time (light gray =early time, dark=later time). In the lower right, there is a region of locally correlated motion. A transient vortex is present in the upper left. Although correlated motion is common, since motion in a dense packing requires motion of neighboring grains, vortices are rare events. In addition, unlike vortices in fluids, there are no inertial effects and granular vortices appear to quickly dissipate without affecting the long-time behavior of the grains.

VIII. CONCLUSIONS

To conclude, we find that granular motion in dense shear flows is diffusive with a self-diffusivity proportional to the local shear rate ($D \approx \dot{\gamma} a^2$, where a is the particle radius). However, the diffusion tensor D is anisotropic due to underlying anisotropies in both the velocity field and force network. The velocity anisotropy leads to a tangential diffusiv-

ity that is about double the radial diffusivity. The anisotropic force network dominates the local diffusivity outside the immediate vicinity of the shearing surface, and leads to a minimum diffusivity approximately along the mean force chain direction. This latter feature has not been observed in more rapid flows, to our knowledge, and is a property of dense granular systems.

Motion can appear subdiffusive due to the decreasing shear rate away from the shearing surface or superdiffusive due to Taylor dispersion effects. A simple random walk model which reproduces the apparent anomalous diffusion indicates that the underlying motion is diffusive. Using the experimentally measured velocity profile, assuming $D_\theta/D_r \approx 2$, and choosing an overall multiplicative scale factor, the simulation closely matches the experiment, including the long-time behavior which is affected by the gradient in shear rate and Taylor dispersion. The simulation also highlights the effects of the anisotropic force network. Differences in the sign of $D_{r\theta}$ between simulation and experiment are associated with the anisotropic force network. The same is true for the orientation of the minimum diffusivity $D_{\phi\phi}$. Velocity autocorrelation plots show that motion in dense granular flows quickly becomes uncorrelated and there is not a distinguishable ballistic regime before diffusive behavior dominates.

Examples of correlated motion, such as vortices, and trajectories similar to Lévy flights are also observed. However, these effects are sufficiently intermittent and random that the system behaves diffusively.

ACKNOWLEDGMENTS

We appreciate a number of very helpful discussions with Professor John Brady. This work was been supported by the National Science Foundation through Grant Nos. DMR-0137119, DMS-0204677, and DMS-0244492, and by NASA Grant No. NAG3-2372.

[1] D. Howell, R. Behringer, and C. Veje, Chaos **9**, 559 (1999).
[2] D. Mueth *et al.*, Nature (London) **406**, 385 (2000).
[3] W. Losert, L. Bocquet, T. Lubensky, and J. Gollub, Phys. Rev. Lett. **85**, 1428 (2000).
[4] G. Barker and A. Mehta, Phys. Rev. E **47**, 184 (1993).
[5] R. Wildman, J. Huntley, and J.-P. Hansen, Phys. Rev. E **60**, 7066 (1999).
[6] J. Seymour, A. Caprihan, S. Altobelli, and E. Fukushima, Phys. Rev. Lett. **84**, 266 (2000).
[7] K.M. Hill, G. Gioia, and V.V. Tota, Phys. Rev. Lett. **91**, 064302 (2003).
[8] S. Hsiau and M. Hunt, J. Fluid Mech. **251**, 299 (1993).
[9] N. Menon and D. Durian, Science **275**, 1920 (1997).
[10] V. Natarajan, M. Hunt, and E. Taylor, J. Fluid Mech. **304**, 1 (1995).
[11] S.-S. Hsiau and Y.-M. Shieh, J. Rheol. **43**, 1049 (1999).
[12] S.-S. Hsiau and W.-L. Yang, Phys. Fluids **14**, 612 (2002).
[13] M.L. Hunt, S.S. Hsiau, and K.T. Hong, J. Fluids Eng. **116**, 785 (1994).
[14] H. Makse and J. Kurchan, Nature (London) **415**, 614 (2002).
[15] F. Radjai and S. Roux, Phys. Rev. Lett. **89**, 064302 (2002).
[16] S.B. Savage and R. Dai, Mech. Mater. **16**, 225 (1993).
[17] V. Garzo, Phys. Rev. E **66**, 021308 (2002).
[18] C. Campbell, J. Fluid Mech. **348**, 85 (1997).
[19] M. Lätzel *et al.*, Eur. Phys. J. E **11**, 325 (2003).
[20] A. Sierou and J. F. Brady, J. Fluid Mech. (to be published).
[21] G. Taylor, Proc. R. Soc. London, Ser. A **219**, 186 (1953).
[22] K. Feitosa and N. Menon, Phys. Rev. Lett. **88**, 198301 (2002).
[23] R. Wildman and D. Parker, Phys. Rev. Lett. **88**, 064301 (2002).
[24] D.E. Elrick, J. Phys. (France) **15**, 283 (1962).
[25] G. Debregeas, H. Tabuteau, and J. di Meglio, Phys. Rev. Lett. **87**, 178305 (2001).
[26] V. Breedveld *et al.*, J. Chem. Phys. **116**, 10529 (2002).
[27] S. Hsiau and M. Hunt, Trans. ASME, Ser. C: J. Heat Transfer **115**, 541 (1993).
[28] M. Scherer, V. Buchholtz, T. Poschel, and I. Rehberg, Phys. Rev. E **54**, R4560 (1996).
[29] M. Marchioro and A. Acrivos, J. Fluid Mech. **443**, 101 (2001).
[30] B. Utter and R. P. Behringer, e-print cond-mat/0402669.
[31] PSM-4 photoelastic coating is purchased from Vishay Measurements Group, Inc., Raleigh, NC.
[32] C. Veje, D. Howell, and R. Behringer, Phys. Rev. E **59**, 739 (1999).
[33] H. Xu, A. P. Reeves, and M. Y. Louge, Rev. Sci. Instrum. **75**, 811 (2004).
[34] K. Batchelor and G. Austral, J. Sci. Ind. Res. **2**, 437 (1949).
[35] J. Klafter, M. Shlesinger, and G. Zumofen, Phys. Today **49**(2), 33 (1996).
[36] T. Solomon, E. Weeks, and H. Swinney, Physica D **76**, 70 (1994).
[37] K. Christensen, A. Corral, V. Frette, J. Feder, and T. Jossang, Phys. Rev. Lett. **77**, 107 (1996); M. Boguñá and A. Corral, *ibid.* **78**, 4950 (1997).